# Automating and Optimizing Reliability-Driven Deployment in Energy-Harvesting IoT Networks

Xiaofan Yu, *Graduate Student Member, IEEE*, Kazim Ergun, *Graduate Student Member, IEEE*, Xueyang Song, Ludmila Cherkasova, *Member, IEEE*, and Tajana Šimunić Rosing, *Fellow, IEEE*

***Abstract*—Recent years have witnessed a significant expansion in Internet-of-Things (IoT) applications. Although the battery energy availability can be improved with energy harvesting, the overall device reliability management has been overlooked in the existing literature. State-of-the-art reliability models of solar panels, electronics and rechargeable batteries show exponential dependence of failures on temperature. This work is the first to develop a comprehensive reliability deployment framework for energy-harvesting IoT networks, reflecting the non-negligible thermal stresses on each hardware component. Our framework improves the reliability on both *pre-deployment and post-deployment* stages. Prior to deployment, given the historical temperature and solar radiation of the region, we formulate a Mixed Integer Linear Program (MILP) to place the minimum number of nodes, while ensuring (i) full target coverage, (ii) complete connectivity, (iii) energy-neutral operation, and (iv) reliability constraints at each deployed node. We propose a polynomial-time heuristic, R-TSH, to approximate the optimal placement in large-scale deployments. While R-TSH optimizes long-term reliability, the prompt temperature or link quality differences from the historical patterns can significantly degrade device reliability after deployment. The post-deployment section of our design consists of a reliability-driven routing algorithm, AODV-Rel, that adapts to real-time environmental and link quality changes. Extensive analysis is done using a real-world dataset from the National Solar Radiation Database. Simulations in ns-3 show that R-TSH meets all reliability constraints even after 5 years of deployment as compared to the state of the art. In addition, it is 2000x faster than the optimal solution, while placing only 28% more nodes. AODV-Rel further extends the minimal operational lifetime by 1.5 and 2.8 months under temperature deviation and wireless interference.**

***Index Terms*—IoT networks, energy harvesting, reliability, sensor deployment, adaptive routing.**

Manuscript received 7 February 2021; revised 13 August 2021 and 3 May 2022; accepted 7 September 2022. Date of publication 20 September 2022; date of current version 7 March 2023. This work was partially supported by Semiconductor Research Corporation task #2805.001, and in part by National Science Foundation under Grants #1911095, #1826967, #1730158, #1527034, #2100237, #2112167, #2003279. This article is an extended version of our conference paper [1] presented at CNSM'2020 [DOI: 10.23919/CNSM50824.2020.9269122]. The associate editor coordinating the review of this article and approving it for publication was S. Clayman. *(Corresponding author: Xiaofan Yu.)*

Xiaofan Yu, Kazim Ergun, Xueyang Song, and Tajana Šimunić Rosing are with University of California at San Diego, La Jolla, CA 92093 USA (e-mail: x1yu@ucsd.edu; kergun@ucsd.edu; xus023@ucsd.edu; tajana@ucsd.edu).

Ludmila Cherkasova is with Arm Research, San Jose, CA 95134 USA (e-mail: lucy.cherkasova@gmail.com).

Digital Object Identifier 10.1109/TNSM.2022.3208083

## I. Introduction

RECENT years have witnessed a rapid deployment of Internet-of-Things (IoT) for environmental monitoring such as in Smart City [2] and Smart Agriculture [3] applications. Experts predict that there will be 29.4 billion IoT devices globally by 2030. Energy harvesting techniques significantly prolong the lifetime of IoT devices [5]. Existing work on the deployment of energy harvesting sensor networks has studied minimizing the deployment cost after ensuring: (i) coverage, i.e., all points of interest (PoIs) are covered, (ii) connectivity, i.e., all devices are directly or indirectly connected to a gateway, and (iii) energy-neutral operation [6], [7].

Although the energy availability can be enhanced with energy harvesting, reliability degradation is often overlooked in existing literature. Even with infinite energy sources, all hardware components degrade over time and ultimately require repair or complete replacement. As reported by Cisco [8], if not managed carefully, maintenance expenditures can account for up to 80% of the total IoT deployment costs. $3.2M/year is spent on administrative labor and technical support due to system failures for every 100,000 devices.

Previous works have shown that the failure rates, as measured by mean-time-to-failure (MTTF, i.e., the expected time to failure), of electronics devices and solar harvesting systems are exponentially related to temperature [9], [10]. The capacity and the power output of batteries also degrade exponentially in hot environments, while the aging status is quantified by the State of Health (SoH) metric [11]. Starting from SoH of 100%, a battery reaches its end of life when SoH decreases to 80% regardless of the remaining charge [12]. Using state-of-the-art reliability models and various chip core temperatures, the MTTF ratio (compared to the MTTF baseline under 25 °C) of electronic devices and the SoH of batteries after 5 years of use are shown in Figure 1.

To the best of our knowledge, a comprehensive reliability deployment framework that includes key hardware components in energy-harvesting IoT networks has not been studied to date. Without such guidelines, reliability-driven deployment and management becomes difficult, especially for outdoor environmental monitoring at extreme temperatures.

In this paper, we develop a comprehensive reliability-driven framework with two stages:

(i) the *pre-deployment stage* optimizes long-term sensor placement to manage the reliability of an energy-harvesting IoT network, (ii) the *post-deployment stage* adjusts routing

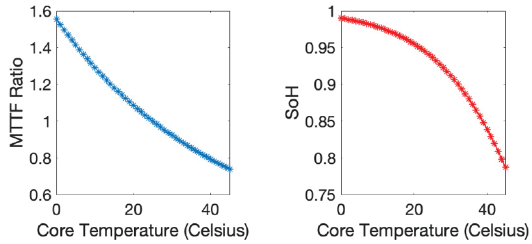


(a) MTTF ratio. (b) SoH after 5 years.

Fig. 1. Impact of chip core temperature on reliability. Higher temperature significantly reduces the reliability.

in real time as a function of environmental and link quality variations. Device placement sets the upper bound on the reliability and useful life of IoT networks. Once deployed, adaptive routing automatically balances the load to approach that upper bound and mitigates unexpected reliability degradations. Both stages consider the effect of environmental conditions (such as temperature and solar radiation) on reliability.

In summary, the contributions of this paper are:

(1) We propose a comprehensive reliability-aware deployment framework for energy-harvesting IoT networks including *pre-* and *post-deployment* stages. We leverage the state-of-the-art reliability models of solar panels, electronics and battery state-of-health, all of which exponentially depend on temperature.

(2) In the *pre-deployment* stage, we formulate a Mixed Integer Linear Program (MILP) for placing the minimal number of sensors, while ensuring (i) reliability, (ii) full coverage of points of interest (PoIs), (iii) complete connectivity, and (iv) energy-neutral operation. We show that the proposed problem is NP-complete, and offer a polynomial-time heuristic, *Reliability-driven Two-Stage Heuristic* (R-TSH) for large-scale deployments.

(3) In the *post-deployment stage*, we design an adaptive routing algorithm, *AODV-Rel*, based on Ad-hoc On-demand Distance Vector (AODV) to dynamically manage reliability in real time. *AODV-Rel* balances reliability in reaction to changes in the environmental conditions or links quality.

(4) We evaluate the benefits of our framework using real-world solar irradiance and ambient temperature dataset from the National Solar Radiation Database (NSRDB) [13]. The experiments are performed both in MATLAB and in *RelIoT*[1] [14], [15], a reliability simulator based on ns-3 [16]. We conduct comprehensive evaluation on the deployment decisions given by R-TSH versus the optimal solution and existing heuristics, and on the adaptive routing algorithm under temperature and link quality variations. Our results indicate R-TSH meets all reliability constraints with 28% more nodes than the optimal solution, but executes 2000x faster. *AODV-Rel* further extends the minimal operational lifetime of deployed nodes by 2.8 months under nearby wireless interference.

[1]*RelIoT* is available at: https://github.com/UCSD-SEELab/RelIoT.

## II. Related Work

### A. Sensor Deployment in Wireless Sensor Networks

Existing literature on sensor deployment mainly optimizes coverage [17], connectivity [18], and network lifetime [19]. All published work optimizing coverage assumes single-use batteries, so their network lifetime is limited. Application requirements can be categorized into area coverage, target coverage, and barrier coverage [20]. The optimization goal is designing a network with a minimum deployment cost or longest lifetime while satisfying the coverage and connectivity requirements [21]. To find the optimal solution, grid placement is transformed into integer programming models and solved with conventional solvers. However, NP-hardness of integer programming problems results in poor scalability, and therefore encourages efficient heuristics [17], [18], [22].

Yang and Chin [6] is the first to formulate a sensor placement problem to achieve energy-neutral operation with the goal of covering fixed targets and ensuring connectivity to the gateway. In addition to using Mixed Integer Linear Programming (MILP) optimization, the authors proposed two greedy heuristics that require 20% and 10% more sensors than their MILP. The later work of Zhu *et al.* [7] considers the placement of directional energy-harvesting sensors for target coverage. They also consider the size of the solar panels at each site as variables that determine the energy harvesting rate. Three heuristics were offered, along with the corresponding analyses on time complexity and performance bound. Nevertheless, neither of [6] or [7] considered reliability, which can cause significant problems in outdoor environments.

### B. Reliability-Driven Network Deployment

Reliability has become increasingly important for large-scale networks that may introduce enormous maintenance costs. Previous works placed redundant nodes to enhance the fault tolerance of the network. Extra nodes can be placed to achieve *k-coverage* (i.e., any point of interest (PoI) needs to be covered by at least $k$ sensors) or *m-connectivity* (i.e., any sensor is required to directly connect to $m$ other nodes). Both strategies temporarily mitigate the negative influence on network functionality upon failures. However, very few existing papers leverage the models of hardware failure mechanisms and address how to preventively reduce the resulting failure rates. Yu *et al.* [23] integrated single-use battery depletion and electronics failure mechanisms to model and optimize maintenance costs in sensor deployments. Their methodology does not apply to energy-harvesting networks.

Our previous work [1] is the first to study reliability-driven deployment in energy-harvesting sensor networks, where the thermal-based reliability models of batteries and electronics are considered. This paper extends and improves [1] in the following ways: (i) it completes the reliability framework for energy-harvesting systems by including thermal-based failure models of solar panels, in addition to device and battery reliability models; (ii) Besides sensor placement optimization prior to deployment, we design an adaptive routing algorithm for dynamic reliability management after deployment; and (iii) a detailed evaluation of the generated deployments and their

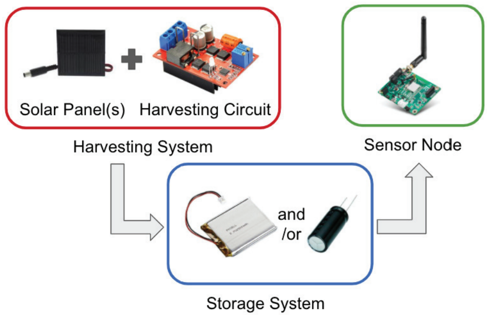


Fig. 2. Components of a solar energy-harvesting system considered in this paper. We consider reliability models for solar panel, electronics and rechargeable batteries.

properties is done with the state of the art ns-3-based reliability simulator *RelIoT* [14], [15] using real-world data.

## III. Reliability Models of Energy-Harvesting Systems

Reliability of a system is the probability $R(t)$ that the system will not fail until time $t$ [9]. It is related to the failure rate of a system, which shows a bathtub curve as a function of time [24]. We focus on the useful lifetime of systems during which the failure rates are constant. Failures in sensor networks can be categorized into link, software, and hardware failures [25]. Both link and software failures can be recovered or avoided with good design. In this paper, we consider permanent *hardware failures* which are very costly, as they require device repair or replacement.

Most energy-harvesting systems leverage the *Harvest-Store-Use Architecture* [5], as shown in Figure 2. The harvesting system includes solar panel(s) and a harvesting circuit for power conversion [26]. The storage system uses supercapacitors and/or rechargeable batteries. We focus on batteries in this work as they have low cycle lifetime, e.g., 1000 cycles [27]. We next introduce the state-of-the-art reliability models for solar panels, electronics and rechargeable batteries.

### A. Solar Panel Reliability Model

Photovoltaic systems have exponential dependence between the failure rate and temperature. We leverage the state-of-the-art reliability model in [10], which is obtained from step-stress aging tests on III-V high concentrator solar cells. The ratio of solar panel's MTTF in comparison to its counterpart under a standard temperature of $T_{ref} = 25°$C is estimated as shown below, where $E_a$ is activation energy and $k$ is Boltzmann constant. $T_{amb}$ is the ambient temperature of the environment.

$$MTTF_{sp}(T_{amb}) = \exp\left[\frac{E_a}{k}\left(\frac{1}{T_{amb}} - \frac{1}{T_{ref}}\right)\right]. \tag{1}$$

### B. Electronics Reliability Model

Previous research has studied common electronics failure mechanisms such as time-dependent dielectric breakdown, negative bias temperature instability, and electromigration, all of which are exponentially dependent on the temperature [9], [28]. We use the term *core temperature* to refer to the internal temperature of a chip. The MTTF for each mechanism can be modeled as a function of time, voltage, temperature, and technological parameters. In [24], the authors showed that the MTTF of all above-mentioned mechanisms share a similar form depending on the core temperature $T_c$. We extract this general expression to estimate MTTF as the ratio to the baseline at $T_{ref} = 25°$C:

$$MTTF_e(T_c) = \exp\left(\frac{E_a}{kT_c}\right) / \exp\left(\frac{E_a}{kT_{ref}}\right), \tag{2}$$

where $E_a$ is the activation energy, $k$ is Boltzmann's constant. According to the thermal dissipation model in [29], $T_c$ linearly depends on average power consumption $P$ of device and ambient temperature $T_{amb}$ at the deployed location:

$$T_c = k_1 P + k_2 T_{amb} + k_3. \tag{3}$$

where $k_1, k_2$ and $k_3$ are device-specific parameters obtained by fitting into experimental traces.

### C. Battery Reliability Model (SoH)

In contrast to the state-of-charge (SoC) model that predicts the available charge in a battery, we utilize the state-of-health (SoH) model, which denotes the aging level of a battery in comparison when it is new. Although a battery can be recharged with harvested energy, it loses its ability to deliver energy, eventually making it unusable. The operational lifetime of a battery is defined as the time when SoH reduces from 1 to 0.8 [12]. Battery aging consists of calendar aging and cycle aging [30]. While calendar aging is exponentially accelerated as a function of time, temperature, and state-of-charge stresses, cycle aging additionally accounts for the degradation due to the depth of discharge (DoD) during each charge-discharge cycle. We use the state-of-the-art semi-empirical SoH model in [12] for Lithium-Ion batteries. Since our goal is to optimize long-term state-of-health, we focus on calendar aging with time and temperature stresses:

$$SoH(t, T_{cell}) = \exp\left\{-k_t\, t \exp\left[k_T\, T_{ref}\left(1 - \frac{T_{ref}}{T_{cell}}\right)\right]\right\}. \tag{4}$$

Here $t$ is the elapsed time since deployment. $T_{cell}$ is the internal battery cell temperature and $T_{ref}$ is the reference temperature of 25 °C. $k_t$ and $k_T$ are predetermined constants. Similar to estimating core temperature, we use the thermal model in [29] to convert ambient temperature $T_{amb}$ to battery cell temperature $T_{cell}$ with different linear coefficients.

## IV. Pre-Deployment Optimization via Sensor Deployment

### A. Sensor Placement Problem Formulation

We assume that sensor nodes can be deployed in a candidate grid space $\mathcal{N}$ to cover a set of points of interest (PoIs) denoted by $\mathcal{O}$. For ease of reading, we list the important symbols used in our formulation in Table I. Assuming at most one device can be placed at a grid point and only one gateway exists, the optimization problem minimizes the number of deployed nodes subject to the following constraints:

TABLE I
LIST OF IMPORTANT NOTATIONS IN PROBLEM FORMULATION

| Symbol | Meaning |
|---|---|
| $\mathcal{N}$ | Set of grid locations |
| $\mathcal{O}$ | Set of point-of-interests |
| $S_c$ | Starting distance of uncertain detection |
| $S_r$ | Feasible sensing radius |
| $C_r$ | Feasible communication radius |
| $p_{th}$ | Required coverage probability threshold |
| $G$ | Quantity of data in each sample |
| $\gamma$ | The maximum possible flow amount |
| $\eta$ | Uniform sampling frequency |
| $BW$ | Communication bandwidth |
| $d_{ij}$ | Euclidean distance between grid $i$ and $j$ |
| $\Gamma_i, \Gamma_B$ | Set of neighbor nodes of node $i$ and the gateway |
| $x_i$ | Whether a device is placed at $i$ |
| $s_i$ | Whether a sensor is placed at $i$ |
| $f_{ij}$ | Average flow quantity from $i$ to $j$ |
| $f_{iB}$ | Average flow quantity from $i$ to the gateway |
| $P_{tx}, P_{rx}$ | Average transmission and reception power |
| $P_i$ | Average power consumption rate at node $i$ |
| $SP_i$ | Approval of solar panel installation at $i$ |
| $P_{SoH,i}$ | Power bound to meet SoH bound at $i$ |
| $P_{MTTF_e,i}$ | Power bound to meet electronics MTTF bound at $i$ |
| $R_i$ | Energy harvesting rate at node $i$ |
| $T_{amb,i}$ | Ambient temperature at node $i$ |
| $T_{cell,i}$ | Battery cell temperature at $i$ |
| $T_{c,i}$ | Internal core temperature at $i$ |
| $T_{ref}$ | Reference temperature of 25 °C |
| $Time$ | Elapsed time for reliability evaluation |

- *Probabilistic coverage constraint:* Each PoI is covered with at least a predetermined probability.
- *Complete connectivity:* All generated data can be successfully routed to the gateway.
- *Energy-neutral operation:* At each deployed site, the energy consumption is less than the harvested energy.
- *Reliability constraints:* Using the models in Section III, the reliability of each deployed device after a predetermined time duration *Time* is greater than a given bound.

The binary variables of the problem are $x_i$ (Eq. (5)) and $s_i$ (Eq. (6)). While $x_i$ suggests whether a device is placed at location *i*, $s_i$ further indicates whether the device performs sensing actions. $x_i$ and $s_i$ enable the problem to distinguish relay nodes (i.e., nodes that only route data) and sensor nodes (i.e., nodes that carry out both sensing and transmission). The continuous variables are $f_{ij}$ and $f_{iB}$ which representing the flow quantity from node *i* to *j* and from node *i* to the gateway.

$$x_i = \begin{cases} 1 \text{ if a device is placed at } i \\ 0 \text{ otherwise.} \end{cases} \tag{5}$$

$$s_i = \begin{cases} 1 \text{ if a sensor is placed at } i \\ 0 \text{ otherwise.} \end{cases} \tag{6}$$

We show an example deployment in Figure 3. Each grid point is a candidate site. The red triangles represent deployed sensor nodes $(x_i = 1, s_i = 1)$ whose sensing radius is shown by the red circle. Both PoIs (green diamonds) are successfully covered by the deployed sensors with level $K = 1$. The blue dots are pure relay nodes $(x_i = 1, s_i = 0)$ that only route data. All nodes are connected to the gateway (orange star).

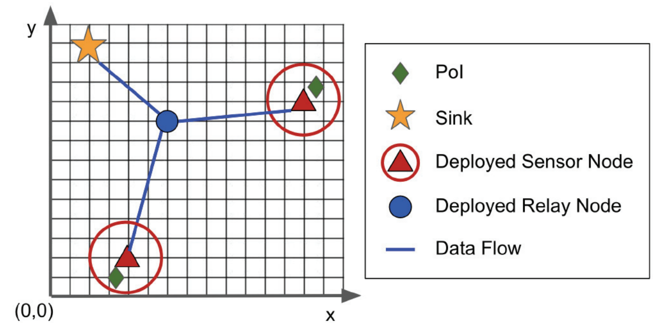


Fig. 3. An example deployment instance.

Now we rigorously formulate the problem as MILP:

$$\min \sum_{i \in \mathcal{N}} x_i \tag{7}$$

subject to

$$\sum_{i \in \mathcal{N}} s_i \cdot \log(1 - cov(i,j)) \leq \log(1 - p_{th}), \quad \forall j \in \mathcal{O} \tag{8a}$$

$$s_i \eta G + \sum_{j \in \Gamma_i} f_{ji} = \sum_{j \in \Gamma_i} f_{ij} + f_{iB}, \quad \forall i \in \mathcal{N} \tag{8b}$$

$$\sum_{i \in \Gamma_B} f_{iB} = \sum_{i \in \mathcal{N}} s_i \eta G \tag{8c}$$

$$s_i \leq x_i, \quad \forall i \in \mathcal{N} \tag{8d}$$

$$\sum_{j \in \Gamma_i} f_{ij} \leq \gamma x_i, \quad \forall i \in \mathcal{N} \tag{8e}$$

$$x_i \leq SP_i, \quad \forall i \in \mathcal{N} \tag{8f}$$

$$P_i \leq \min\{R_i, P_{SoH,i}, P_{MTTF_e,i}\}, \forall i \in \mathcal{N} \tag{8g}$$

$$x_i \in \{0,1\}, s_i \in \{0,1\}, \quad \forall i \in \mathcal{N} \tag{8h}$$

$$0 \leq f_{ij} \leq \gamma, \quad \forall i \in \mathcal{N}, j \in \mathcal{N}, i \neq j \tag{8i}$$

Eq. (8a)-(8g) are deployment constraints that we will explain next. Eq. (8h) and (8i) give the lower and upper limits for all variables.

*Probabilistic Coverage Constraint:* Targeting at general applications, we employ the state-of-the-art probabilistic coverage model for wireless sensor networks [21], [31]. Suppose that *d*(*i*, *j*) represents the Euclidean distance between $i \in \mathcal{N}$ and $j \in \mathcal{O}$. The probabilistic coverage model is defined as:

$$cov(i,j) = \begin{cases} 1 & \text{if } d(i,j) \leq S_c, \\ e^{-\omega \cdot d(i,j)} & \text{if } S_c < d(i,j) \leq S_r, \\ 0 & \text{otherwise.} \end{cases} \tag{9}$$

where $S_c$ is the starting distance of uncertainty in detection, and $S_r$ is the maximal sensing radius. We require the overall detection probability of target $j \in \mathcal{O}$ to be at least a predetermined threshold $p_{th}$:

$$p_j = 1 - \prod_{i \in \mathcal{N}} (1 - s_i \cdot cov(i,j)) \geq p_{th}. \tag{10}$$

By applying the log operation on both sides and following similar derivations as in [32], we are able to convert the product of probabilities into sum, as shown in Eq. (8a). Since the probabilities of *cov*(*i*, *j*) can be computed in advance, Eq. (8a) is a linear constraint.

*Connectivity Constraint:* To account for a variety of modern wireless communication technologies, we model the connectivity with a maximal reachable distance which can be set according to the technology and transmission power. We assume the feasible communication range of each device to be $C_r$. Then the neighbor set $\Gamma_i$ of grid node *i* is defined as $\Gamma_i = \{j \in \mathcal{N} \mid d_{ij} < C_r, j \neq i\}$, where $d_{ij}$ denotes the Euclidean distance between grid locations *i* and *j*. $\Gamma_B$ represents a set of gateways neighbors. The connectivity constraints require: (i) flow conservation, i.e., the sum of the outgoing flow should equal to the sum of the incoming flow and generated data (if any) at each node (Eq. (8b)), (ii) complete connectivity, i.e., all data generated from end devices converge into the gateway (Eq. (8c)). Eq. (8d) and (8e) are feasibility constraints. The former equation states that a sensor can only be placed at the site where a device exists, while the latter one claims that no flow can pass through node *i* if no device is located there. $\gamma = \eta G|\mathcal{N}|$ is defined as the maximum flow quantity possible in the network.

*Energy-Neutral Operation Constraint:* To achieve energy-neutral operation at each deployed spot, the average power of the device should be less than or equal to the harvesting rate. Energy-harvesting sensor node consumes ambient power (e.g., dissipated power during sleep state), sensing power, and communication power [33]. We assume that the system wakes up once in a sampling interval $T_{cycle}$, performs the sensing task, transmits the packet, and sleeps again before the next cycle. The average power of a device at grid *i* is then:

$$P_i = P_0 + s_i E_s \eta + \sum_{j \in \Gamma_i} \left( P_{tx}(d_{ij}) \frac{f_{ij}}{BW} + P_{rx} \frac{f_{ji}}{BW} \right), \tag{11}$$

where $P_0$ is a constant that denotes the dissipation of ambient power. $E_s$ is the energy consumed per sensing task and $\eta = 1/T_{cycle}$ is the sampling frequency. Thus, $E_s\eta$ stands for the average power in sensing. With $s_i$, sensing power is only counted when a sensor is placed at *i*. The last term in the bracket is the average transmission and reception power models using typical parameters for BPSK [34]. The transmission power varies polynomially with the distance: $P_{tx}(d) = p_{to} + k \cdot d^{\alpha}$, where $p_{to}, k$ and $\alpha$ are predefined constants. The average reception power $P_{rx}$ is fixed. *BW* is the bandwidth limitation.

The average energy harvesting rate $R_i$ at grid location *i* can be determined by the average solar irradiance level $\lambda_i$ (W/m$^2$) [7]: $R_i = \xi_i A \lambda_i$, where *A* is the surface area of the solar panel, $\xi_i$ is the end-to-end conversion efficiency of the solar system at node *i*. $\lambda_i$ is available from online databases such as NSRDB [13]. We assume uniform *A* among all deployed nodes in our formulation. $\xi_i$ depends linearly on ambient temperature $T_{amb,i}$ and solar irradiance level $\lambda_i$ at node *i* [35]:

$$\xi_i = aT_{amb,i} + aR_{th}\lambda_i + b, \tag{12}$$

where $R_{th}$ is the thermal resistance of solar panel and *a*, *b* are predetermined constants. $a, b, R_{th}$ are obtained from experimental measurements. Combining the above components, we write the energy-neutral operation constraint at *i* as $P_i \leq R_i$.

*Reliability Constraints:* We now explain how to convert the nonlinear reliability models in Section III to linear constraints. All reliability models rely on the distribution of ambient temperature, $T_{amb}$, at the specific location. The expectation of reliability at a specific location *i* can be calculated as in Eq. (13), where $p_{T_{amb,i}}$ is the probability associated with the temperature distribution at location *i*.

$$\overline{MTTF_{sp,i}} = \int_{-\infty}^{\infty} MTTF_{sp}(T_{amb,i}) p_{T_{amb,i}} dT_{amb,i} \tag{13a}$$

$$\overline{SoH_i} = \int_{-\infty}^{\infty} SoH(T_{cell,i}(T_{amb,i}, P_i)) p_{T_{amb,i}} dT_{amb,i} \tag{13b}$$

$$\overline{MTTF_{e,i}} = \int_{-\infty}^{\infty} MTTF(T_{c,i}(T_{amb,i}, P_i)) p_{T_{amb,i}} dT_{amb,i} \tag{13c}$$

The solar-panel reliability model depends only on ambient temperature (Eq. (1)) thus $\overline{MTTF_{sp,i}}$ is fully determined given a temperature distribution. If high ambient temperature puts the MTTF ratio of the solar panel below a reference value $MTTF_{sp,ref}$, we label the current location as unsuitable for deploying solar panels. We introduce the notation $SP_i$ to indicate whether the solar panel can be installed at a particular location:

$$SP_i = [\overline{MTTF_{sp,i}} \geq MTTF_{sp,ref}]. \tag{14}$$

Here, the notation [*Cond*] gives 1, when the inner condition *Cond* is met; otherwise 0. With $SP_i$, we specify the solar panel reliability constraint at each site *i* as Eq. (8f).

For electronics and battery reliability, we require $\overline{SoH_i}$ and $\overline{MTTF_{e,i}}$ to satisfy reference thresholds:

$$\overline{SoH_i} \geq SoH_{ref} \tag{15a}$$

$$\overline{MTTF_{e,i}} \geq MTTF_{e,ref} \tag{15b}$$

Note that after the integral in Eq. (13), the expectations of SoH and MTTF only rely on the average power of the device at location *i*. Given the distribution of ambient temperature, $\overline{SoH_i}$ and $\overline{MTTF_{e,i}}$ monotonously decrease with $P_i$. Therefore we can determine the corresponding upper bounds on the average power to meet the reliability constraints. We employ the binary search algorithm to efficiently estimate the power upper bound caused by battery SoH and electronics MTTF constraints (i.e., $P_{SoH,i}$ and $P_{MTTF_e,i}$) within a precision of $\varepsilon$. Initiating the two ends of search space to 0 and $P_{max}$, it takes at most $log_2(\lceil \frac{P_{max}}{\varepsilon} \rceil)$ iterations to locate the desired power bound.

Since both the energy-neutral operation and reliability constraints are expressed as power upper bounds, they can be combined into one single linear inequality as in Eq. (8g).

*Complexity Analysis:* The number of decision variables in the formulated MILP is $2|\mathcal{N}| + |\mathcal{N}|^2$, where $2|\mathcal{N}|$ of them are binary and the rest $|\mathcal{N}|^2$ variables are continuous. After simplification, we arrive at $|\mathcal{N}| + 1$ equality constraints and $3|\mathcal{N}| + |\mathcal{O}|$ inequality constraints. We implement and solve the proposed problem in CPLEX 12.10 [36]. However, the proposed problem cannot be solved in polynomial time since it is NP-complete.

First, the problem belongs to the class of NP. For any given instance, we can verify whether it satisfies Eq. (8a)-(8g) in polynomial time. Then, we consider a relaxed version of (P) by setting $G = 0, P_0 = 0, E_s = 0, P_{tx} = P_{rx} = 0$. Namely, we relax the flow, power and reliability constraints as arbitrary values of $f_{ij} < \gamma$ can satisfy the above constraints. With only the coverage constraints, the relaxed problem is equivalent to the minimum set cover problem whose goal is to find a cover for a given set of targets $\mathcal{O}$ with the minimum number of grid points from $\mathcal{N}$. Hence, the proposed problem is reducible to a well-known NP-complete problem of minimum set cover [37]. It is also clear that arbitrary instances of set covering can be encoded as an instance of the proposed problem. Therefore the proposed problem is NP-complete.

### B. Proposed Heuristic: R-TSH

Given that our optimization problem is NP-complete, we design a heuristic, *Reliability-driven Two-Stage Heuristic* (R-TSH) for large-scale problems. We add reliability constraints to the Two-Stage Heuristic (TSH) proposed in [7]. In contrast to TSH [7] which attempts to minimize the deployment cost, R-TSH disables a node *i* which violates solar panel MTTF constraints (Eq. (8f)), and makes selections based on the equivalent power bound $P_{bd,i} = \min\{R_i, P_{SoH,i}, P_{MTTF_e,i}\}$ to address the electronics MTTF and the battery SoH requirements. In this way, R-TSH meets the reliability constraints and ensures energy-neutral operation. The complete flow of R-TSH is shown in Algorithm 1.

**Algorithm 1** R-TSH

**Input:** $\mathcal{N}, \mathcal{O}, c, K, SP, P_{bd,i}$
**Output:** $\mathcal{X}, \mathcal{S}, \mathcal{F}$

1: $\mathcal{S} \leftarrow \varnothing$ ▷ selected sensor node set
2: $\mathcal{U} \leftarrow \{1, 2, \ldots, |O|\}$ ▷ PoIs not fully covered
3: $q_i \leftarrow K, \forall i \in \mathcal{N}$ ▷ unsatisfied coverage requirements
4: $\mathcal{N} \leftarrow \{i \mid SP_i = 1, i \in \mathcal{N}\}$ ▷ filter out unapproved sites
5: **while** $\mathcal{U} \neq \varnothing$ **do**
6: $\quad \mathcal{S}_i \leftarrow \sum_{j \in U} cov(i,j), \forall i \in \mathcal{N}$ ▷ PoIs covered by $i$
7: $\quad i^* \leftarrow arg\,max\{|\mathcal{S}_i \cap \mathcal{U}| \cdot P_{bd,i} \mid i \in \mathcal{N} - \mathcal{S}\}$
8: $\quad$ **if** $|\mathcal{S}_{i^*} \cap \mathcal{U}| = \varnothing$ **then**
9: $\quad\quad$ **break** ▷ no new coverage
10: $\quad$ **end if**
11: $\quad$ **for all** $k \in |\mathcal{S}_{i^*} \cap \mathcal{U}|$ **do**
12: $\quad\quad q_k \leftarrow q_k - 1$
13: $\quad\quad$ **if** $q_k \leq 0$ **then**
14: $\quad\quad\quad \mathcal{U} \leftarrow \mathcal{U} - \{k\}$
15: $\quad\quad$ **end if**
16: $\quad$ **end for**
17: $\quad \mathcal{S} \leftarrow \mathcal{S} \cup \{i^*\}$ ▷ update sensor node set
18: **end while**
19: **if** $\mathcal{U} \neq \varnothing$ **then**
20: $\quad$ **return** Null ▷ infeasible in full coverage
21: **end if**
22: $\mathcal{V} \leftarrow \{\mathcal{N}, c\}, \mathcal{E} \leftarrow \{(i,j) \mid i,j \in \mathcal{V}, i \neq j, j \in \Gamma_i\}$
23: $\mathcal{W}(i,j) \leftarrow \omega_1[i \notin \mathcal{S}] + \omega_2 \frac{(P_{tx}(d_{ij}) + P_{rx})\eta G/BW}{P_{bd,i} - (P_0 + E_s \eta[i \in \mathcal{S}])}, \forall (i,j) \in \mathcal{E}$
24: $\mathcal{GP} \leftarrow \texttt{CreateGraph}(\mathcal{V}, \mathcal{E}, \mathcal{W})$
25: $\mathcal{F} \leftarrow \texttt{ShortestPathTree}(\mathcal{GP}, \mathcal{S}, c)$
26: $\mathcal{X} \leftarrow \{i \mid i \in \mathcal{F}\}$
27: **return** $\mathcal{X}, \mathcal{S}, \mathcal{F}$

R-TSH first filters out the sites that violate solar-panel reliability constraints (line 4). Next it selects the nodes that satisfy SoH and electronics MTTF constraints in two stages. The first sensor selection stage (line 4 - 20) selects the sensor locations with the maximum benefit:

$$Benefit_i = |\mathcal{S}_i \cap \mathcal{U}| \cdot P_{bd,i} \tag{16}$$

where $\mathcal{S}_i$ denotes the set of PoIs covered by location *i* and $\mathcal{U}$ represents the PoIs that have not been fully covered. The benefit function favors locations that cover more PoIs while meeting power bounds. The selecting loop exits once the probabilistic coverage is attained, or no new coverage can be made. The latter case indicates that the problem is infeasible.

The second stage focuses on the communication-path selection. Here we construct a directed graph $\mathcal{GP}$ by including all connectable edges and assign the following weight to edge (*i*, *j*) with tuned parameters $\omega_1, \omega_2$:

$$\mathcal{W}(i,j) \leftarrow \omega_1[i \notin \mathcal{S}] + \omega_2 \frac{(P_{tx}(d_{ij}) + P_{rx})\eta G/BW}{P_{bd,i} - (P_0 + E_s\eta[i \in \mathcal{S}])} \tag{17}$$

The first term appends additional cost to the edge if *i* is not added to the sensors set $\mathcal{S}$ in stage 1. The second term computes the ratio of increased transmission power and remaining power budget. Intuitively, the communication paths costing less transmission power and less critical in energy bounds as well as reliability constraints are given higher priorities. Dijkstra's algorithm is used to concurrently find the shortest paths $\mathcal{F}$ from selected sensors $\mathcal{S}$ to the gateway $c$ in $\mathcal{GP}$ (line 25). All selected sensor nodes and relay nodes are returned in $\mathcal{X}$. The routing graph is captured by $\mathcal{F}$.

*Complexity Analysis:* The initialization from line 1 to 3 is $O(|\mathcal{O}| + |\mathcal{N}|)$. The while-loop in line 4 takes at most $K|\mathcal{O}|$ iterations. If the matrix of *cov*(*i*, *j*) is calculated and stored in advance, both line 5 and 6 cost $O(|\mathcal{N}|)$ time. The for loop in line 10 consumes $O(|O|)$ time. Hence the time complexity of the first stage (line 4 - 10) is $O(K|\mathcal{N}||\mathcal{O}|)$. In the second stage (line 21 - 25), the constructed graph is sparse. Suppose that the feasible communication radius is $C_r$ and the distance between the two adjacent sites is *d*. Then one site can connect to at most $(2\lfloor \frac{C_r}{d} \rfloor + 1)^2$ other nodes including the sink. We denote this constant as *C*. The number of edges in the graph should satisfy $|\mathcal{E}| < C|\mathcal{N}|$. Constructing a graph with $|\mathcal{N}|$ vertices and $|\mathcal{E}|$ edges takes $O(|\mathcal{N}| + |\mathcal{E}|) = O(|\mathcal{N}|)$. Applying Dijkstra's algorithm to find the shortest path takes $O(|\mathcal{E}| + |\mathcal{N}| \log |\mathcal{N}|) = O(|\mathcal{N}| \log |\mathcal{N}|)$ time. Therefore, the overall time complexity of R-TSH ends up with $O(K|\mathcal{N}||\mathcal{O}| + |\mathcal{N}| \log |\mathcal{N}|)$.

## V. Post-Deployment Optimization via Routing

While R-TSH jointly optimizes sensor deployment and routing paths considering temperature and solar irradiance distributions, we recognize that practical conditions can affect the performance after deployment. The deployed sensors might experience unexpected heat waves resulting in more severe

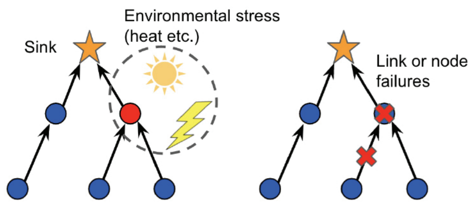


Fig. 4. Post-deployment changes that motivate adaptive routing.

reliability degradation than R-TSH's estimates. Lower than expected solar energy availability may cause service outages. Unreliable communication and random node failures are typical of sensor network deployments. To combat these post-deployment changes (as shown in Figure 4), we propose an adaptive routing algorithm based on Ad-hoc On-demand Distance Vector (AODV) [38] as the second component of our reliability-driven framework. The goal is to balance reliability degradation due to varying conditions and alleviate the negative impacts of potential failures after deployment.

### A. Adaptive Routing Algorithm: AODV-Rel

AODV routing protocol is a decentralized and reactive protocol for ad-hoc networks, which has been shown to consume less energy than its counterparts [39]. AODV detects and adapts to changes in the network in a timely manner by exchanging Route Requests (RREQ) and Route Replys (RREP) between nodes. Our adaptive routing algorithm, *AODV-Rel* is based on AODV to leverage the adaptive mechanism of AODV to address post-deployment changes during runtime.

With AODV, each node maintains a routing table obtained from request-response cycles among the network. The routing table records the next hop with its latest routing cost. All packets are forwarded to the next hop with minimal routing cost. In the original AODV, the routing cost is simply the number of hops to transmit from one node to the other. *AODV-Rel* instead relies on reliability-aware cost metric to balance reliability degradation. Suppose that the routing cost from node $u$ to the sink (node *0*) is $Q_u$. The routing table at node $u$ documents the aggregated routing cost collected from its neighbors and selects the next destination as the node with the minimal routing cost:

$$arg\ min_{v\in\Gamma_u} Q_v + \exp\big(-M_{u,v,t}\big), \tag{18}$$

where $\exp(-M_{u,v,t})$ is a reliability-aware cost metric between nodes $u$ and $v$ that distinguishes our design from the original AODV. $M_{u,v,t}$ denotes the power margin to choose a hop $u$ to $v$ at time $t$.

The power margin metric should accurately capture the reliability degradation due to environmental stresses and link failures. We propose to compute the power margin as follows:

$$M_{u,v,t} = P_{bd,u,t} - P_{cur,u,t} - (P_{tx}(d_{uv}) + P_{rx})\eta G/BW. \tag{19}$$

The power bound $P_{bd,u,t} = \min\{R_{u,t}, P_{SoH,u,t}, P_{MTTF_e,u,t}\}$ is similar as we used in R-TSH, which reflects the maximal allowed power to meet (i) energy-harvesting, (ii) SoH, and (iii) electronics MTTF constraints under *real-time* environmental conditions. Notice, that different from the pre-deployment optimization, the power bound metric here records the real-time status rather than long-term expectation. The second term $P_{cur,u,t}$ is the current power measurement under *real-time* link conditions. We assume that retransmissions are initiated until the packets are successfully received or a maximum number of retransmissions is reached. Poor link quality causes more retransmissions and increases the average power. The third term in Eq. (19) denotes the increased power if link $u$ to $v$ is selected, which also appears in Eq. (17).

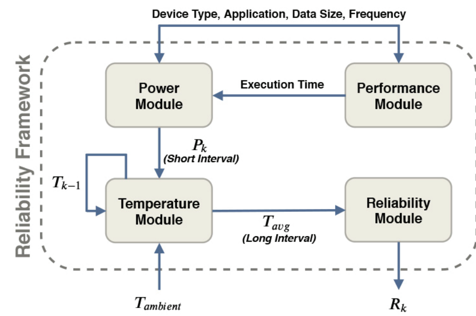


Fig. 5. Reliability framework in *RelIoT*.

The proposed reliability-aware power margin metric includes all potential reliability degradation sources as depicted in Figure 4. Environmental changes of temperature and solar irradiance push the real-time power bound $P_{bd,u,t}$, while poor link qualities increase the current power $P_{cur,u,t}$, both closing the power margin $M_{u,v,t}$. In addition, the power cost of transmitting from $u$ to $v$ due to distance is also integrated in $M_{u,v,t}$. We use the exponential form of negative power margin to favor large margins and impose an exponential penalty on negative margins.

### B. Implementation

We implement *AODV-Rel* in *RelIoT* [14], an open-source reliability simulation framework based on ns-3 [16]. While ns-3 provides discrete event-based simulations for networking, *RelIoT* further provides power, temperature, and reliability modules for analysis, as shown in Figure 5. In contrast to the model-based MATLAB simulations, *RelIoT* offers more dynamism as it simulates the protocol-based packet delivery and reliability degradation under real-time temperature and solar radiation traces. Specifically, the simulator has a state-based module that alternates between communication states, TX, RX, IDLE, SLEEP with varying durations, which results in different amounts of power and energy consumption throughout the simulation.

In *RelIoT*, we configure the power and temperature modules according to the models described in Section III and Section IV. We also utilize the energy harvesting and battery modules of ns-3 to monitor battery capacities over the simulation horizon and validate energy-neutral operation. To account for environmental conditions, we download the hourly ambient temperature and solar radiation traces from NSRDB [13], and input them to the temperature module and the energy

TABLE II
PARAMETER SETTINGS IN EVALUATION

| Param. | Value | Param. | Value | Param. | Value |
|---|---|---|---|---|---|
| $S_c$ | 100 m | $S_r$ | 120 m | $C_r$ | 200 |
| $G$ | 100 B | $BW$ | 2000 B/s | $P_0$ | 0.01 W |
| $E_s$ | 0.04 J | $P_{to}$ | 0.22 W | $\beta$ | $10^{-7}$ |
| $\alpha$ | 3.5 | $P_{rx}$ | 0.1 W | $A$ | 0.01 $m^2$ |
| $\xi$ | 0.05 | $\eta$ | 0.1 | $\omega_1, \omega_2$ | 1, 1.3 |

harvesting module, respectively. Finally, we introduce two functions to *RelIoT* for computing electronics MTTF and SoH using the core temperature traces obtained from the temperature module. The simulator estimates electronics reliability using the Time-Dependent Dielectric Breakdown (TDDB) model [9], [28].

With the above configuration, we are able to estimate the time-wise reliability per deployed node. *AODV-Rel* is then implemented based on the AODV module in ns-3, using the routing cost defined in Eq. (18).

## VI. EVALUATION

In this section, we first present the simulation setup (Section VI-A). The numerical results in MATLAB on sensor placement are listed in Section VI-B. Then Section VI-C provides the ns-3 based *RelIoT* [14], [15] simulation results including both sensor placement and adaptive routing. Finally, we explicitly discuss the impact of parameters on reliability trade-offs in Section VI-D.

### A. Simulation Setup

We solve the MILP with CPLEX 12.10 [36] and then compare to our heuristic in MATLAB R2020b. The source code for our algorithms is available online.[2] Simulation experiments are performed on a Linux desktop with Intel Core i7-8700 CPU at 3.2 GHz and 16 GB RAM. We use a dataset covering 100 km × 100 km region in Southern California, downloaded from NSRDB [13]. The dataset contains half-hourly solar irradiance and ambient temperature measurements across multiple years. We project the spatial temperature distribution to the candidate grid space over a variety of field sizes. The positions of PoIs and the gateway are randomly initialized. We set the reliability bounds $MTTF_{sp,ref} = 1.33, SoH_{ref} = 0.9, MTTF_{e,ref} = 0.9$ and elapsed time *Time* = 5 years. Table II reports the detailed parameter settings.

The communication-related parameters used in *RelIoT* are summarized in Table III. We set multicast routing between nodes with Constant Bit Rate (CBR) traffic, conforming to the flow rates and routes described by the deployment.

The performance of the following methods are evaluated:

- *OPT:* The optimal solution to the proposed problem.
- *OPT$_{noRel}$:* The optimal solution to the proposed problem without the reliability constraints.
- *R-TSH:* Our proposed heuristic.

We select two baselines from [7] to compare with: (1) *TSH*, the original two-stage heuristic, and (2) *SRIGH*, the sensing-

[2]The source code is available at https://github.com/Orienfish/EH-deploy.

TABLE III
NS-3 SIMULATION PARAMETERS

| **Parameter** | **Value** |
|---|---|
| Routing Protocol | Static Routing |
| MAC Layer | IEEE 802.11b |
| Traffic Type | CBR UDP |
| Data Rate | 1 kBps per sensor |
| Packet Size | 1024 bytes |
| Bandwidth | 1Mbps |
| Loss Model | Friis Propagation Loss Model |

and routing- integrated greedy heuristic in [7]. SRIGH greedily selects a sensing node and its communication route within each iteration, thus fails to balance routing from a global view. Both TSH and SRIGH are devised to cover PoIs with minimum deployment cost while ensuring energy-neutral operation.

### B. Numerical Results on Sensor Placement

*1) Small-Scale Problem Simulations:* We perform small-scale problem simulations on a grid space of 500 m × 500 m and set the desired coverage probability to $p_{th} = 0.6$.

*Various number of PoIs:* First, we set the number of candidate grid sites to 100 and choose the number of PoIs from 5 to 25. Since the positions of PoIs are initialized randomly, we run all methods with 40 different initializations and calculate the average result with 90% confidence interval. Figure 6a displays the number of deployed nodes and reliability violations (i.e., the portion of deployed nodes that violate at least one of the reliability bounds) of each method in our simulation. OPT deploys 49% more nodes than OPT$_{\mathbf{noRel}}$ to satisfy the reliability constraints. However, if optimizing without the reliability, OPT$_{\mathbf{noRel}}$ will have more than 53% of nodes violating the reliability bounds. Our heuristic R-TSH deploys around 28% more nodes than OPT but it is more than 2000x faster while keeping reliability violation below 4%. Note, that R-TSH adjusts trade-off between the number of deployed nodes and reliability violations by $\omega_1$ and $\omega_2$, which is discussed in Section VI-D. R-TSH picks 13% and 63% more nodes than TSH and SRIGH but TSH and SRIGH have 14% and 24% violations on average respectively.

*Various number of candidate sites:* In the second experiment,set PoIs to 20 and select the number of candidate grid sites from $\{100, 110, 120, 130, 140\}$. Figure 6b presents the average number of nodes and reliability violations after 40 random trials. Similar improvements can be observed in all three sets of comparisons. Additionally, comparing Figure 6a and Figure 6b, we see that the number of deployed nodes is driven sublinearly by PoIs. Creating finer-grained candidate sites can improve the quality of solutions by satisfying the same constraints with fewer nodes at the cost of longer execution time.

*2) Large-Scale Problem Simulation:* We next evaluate a grid space of 5 km × 5 km to compare the performance of R-TSH and two heuristic baselines in a larger setting. The coverage level is $p_{th} = 0.9$. We report the performances of R-TSH, TSH, and SRIGH, with varying the number of PoIs and grid locations in the field. The average results of

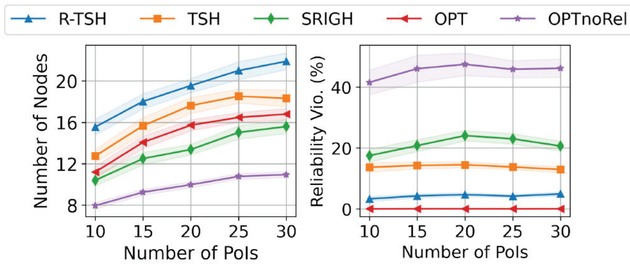


(a) Numerical results with various number of PoIs to cover. Left: the minimum deployed nodes. Right: reliability violations.

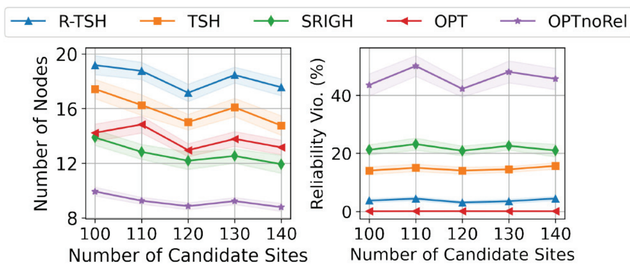


(b) Numerical results with various number of candidate sites. Left: the minimum deployed nodes. Right: reliability violations.

Fig. 6. Numerical results with 90% confidence interval on a small-scale problem.

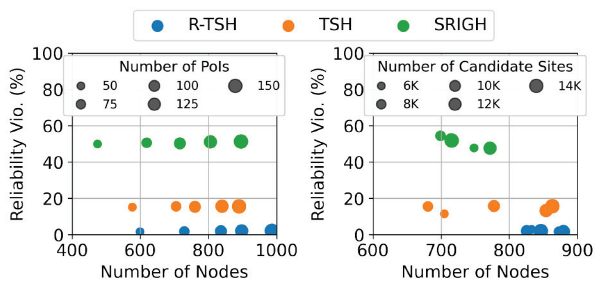


(a) The minimum deployed nodes and the percentage of reliability violations on a large field. Left: when varying number of PoIs. Right: when varying number of candidate sites.

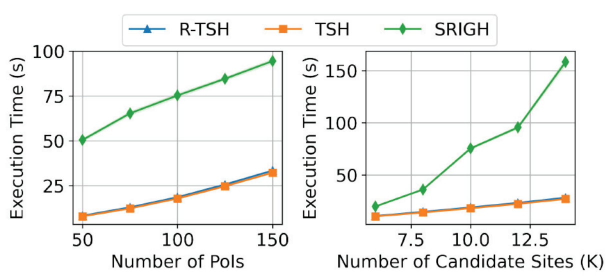


(b) Execution time results. Left: the execution time when varying number of PoIs. Right: the execution time when varying number of candidate sites.

Fig. 7. Numerical results on a large-scale problem.

40 randomly initialized cases are shown in Figure 7a and Figure 7b.

*Various number of PoIs:* We place 10K candidate sites in the field while varying the number of PoIs from 50 to 150. Figure 7a (left) scatters the number of deployed nodes and reliability violations of all heuristics while altering the number of PoIs to be covered. It can be seen that R-TSH places 6% and 16% more nodes on average than TSH and SRIGH respectively, but both baselines result in 17% or more reliability violations.

*Various number of candidate locations:* We next set the number of PoIs to 100 and change the candidate grid size. Figure 7a (right) shows the results as the number of candidate locations changes from 6K to 14K. Reliability violations of TSH and SRIGH fluctuate from 15% to 55% when the size of the grid space changes. At the same time, R-TSH consistently keeps the violation rates below 3% while having 10% and 16% more nodes than TSH and SRIGH respectively. Interestingly, R-TSH returns much better solutions than TSH on both metrics, the number of deployed nodes and reliability, when the number of candidate sites is more than 12K.

*Execution Time:* Figure 7b displays the execution time of all heuristics in the above two experiments. R-TSH and TSH consume similar time as they adopt the same mechanism, which is different from SRIGH. The runtime of R-TSH and TSH increases as more PoIs or candidate sites are considered, which agrees with our complexity analysis in Section IV-B. SRIGH runs much longer than R-TSH and TSH, especially with more candidate sites. This can be attributed to the fact that SRIGH calls the Dijkstra's algorithm multiple times to update routing path along with the node selection, while the two-stage mechanisms only trigger it once.

### C. RelIoT (ns-3) Results

*1) Sensor Placement in Pre-Deployment Stage:* For more realistic validation, we evaluate the same networks with the same setup as shown in the previous section by using state-of-the-art reliability, power, and performance simulator *RelIoT*. We input the temperature and solar irradiance traces from NSRDB into the simulator, bringing more realistic dynamism to the simulation.

Similar as the small-scale deployment, we randomly initialize PoIs over a grid of 500 m $\times$ 500 m, generate deployment plans with all methods, and simulate the established networks. The number of nodes deployed, the minimum SoH, and the minimum electronics MTTF of the nodes for the 5-year simulation time and each deployment method are given in Table IV. SoH and MTTF values are represented as percentages with respect to their standard values at temperature $T_{ref} = 25$°C. The minimum SoH and MTTF usually occur on the same node which acts as a root in the routing topology. This node degrades faster as it does a lot of the routing of traffic. We refer to it as the *bottleneck node*.

As shown in Table IV, $\text{OPT}_{\textbf{noRel}}$ deploys fewer nodes than the other methods, but causes unbalanced reliability in the network. The bottleneck node in $\text{OPT}_{\textbf{noRel}}$ violates the SoH and electronics MTTF bounds, i.e., $SoH_{ref} = 0.9, MTTF_{e,ref} = 0.9$. Only reliability-driven methods, OPT and R-TSH, are able to meet the reliability bounds. R-TSH deploys 13% more nodes than OPT. Compared with the baseline heuristics, R-TSH deploys approximately 25% more nodes.

TABLE IV
COMPARISON OF THE DEPLOYMENTS GENERATED BY VARIOUS METHODS IN *RelIoT*

| Method | Number of Nodes | Min SoH | Min MTTF$_e$ |
|---|---|---|---|
| OPT$_{\mathbf{noRel}}$ | **15** | 81.2% | 79.1% |
| SRIGH | 19 | 87.1% | 88.2% |
| TSH | 20 | 89.6% | 93.9% |
| OPT | 22 | 90.1% | 94.7% |
| R-TSH | 25 | **90.1%** | **95.0%** |

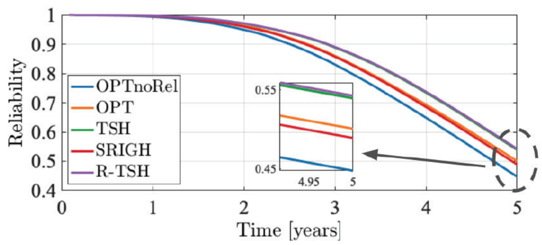


(a) Time-wise TDDB reliability on the bottleneck node of each deployment in 5 years.

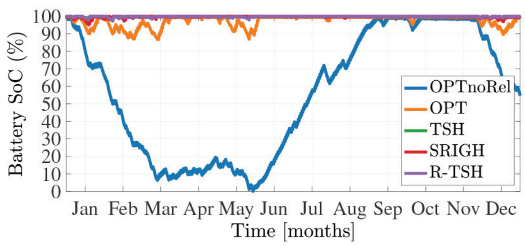


(b) Time-wise battery SoC on the bottleneck node of each deployment in 1 year.

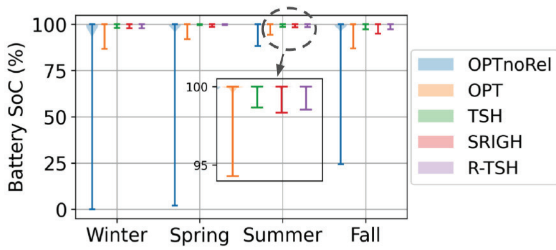


(c) Season-wise distribution of battery SoC on all nodes of each deployment in 1 year.

Fig. 8. Time-wise simulation results in *RelIoT*.

*TDDB reliability degradation:* To examine the reliability degradation mechanism in more details, we plot the reliability of electronics computed internally by *RelIoT* for the bottleneck node in each deployment in Figure 8a. *RelIoT* leverages the TDDB model [9], [28], which defines reliability as the probability of not having failures before a given time $t$ and takes the values in the range [0, 1]. Figure 8a shows that initially the reliability for all methods is similar but the difference is exacerbated over time due to the exponential dependency. By the end of the 5-year duration, the bottleneck node in OPT has 12% higher reliability than the bottleneck node in OPT$_{\mathbf{noRel}}$. Furthermore, R-TSH achieves the best reliability among all methods, improving reliability by 11% compared to SRIGH at bottleneck nodes after 5 years.

*Battery State of Charge (SoC):* We also observe the time-wise changes in battery SoC using *RelIoT* to assess how solar panels affect network operation. In Figure 8b, we show the battery SoC in percentages of the bottleneck node for each method. For all methods except OPT$_{\mathbf{noRel}}$, nodes can recover the depleted battery charge very quickly using energy harvesting. For the bottleneck node in OPT$_{\mathbf{noRel}}$ deployment, energy-neutral operation is still satisfied, although the battery SoC is recovered over a much longer time frame. During cloudy times, there is not much solar energy generation so the battery capacity decreases drastically, but in summer it balances out and goes back to full charge for energy neutral operation.

Figure 8c visualizes the distribution of battery SoC among all nodes for each season. Most nodes maintain a high battery SoC of more than 98%, while OPT$_{\mathbf{noRel}}$ has dramatic variations between minimum and maximum SoC, primarily due to bottleneck nodes whose SoC drops close to zero. Due to season-wise variations in available solar radiation, such bottleneck nodes have higher SoC during summer, but are prone to energy drain during winter. All deployments generated by heuristics preserve high and balanced SoC on all nodes. In summary, the simulation results in *RelIoT* show that OPT$_{\mathbf{noRel}}$ sacrifices reliability, while reliability-driven methods better balance reliability with routing workloads.

*2) Adaptive Routing in Post-Deployment Stage:* While R-TSH is highly optimized for the historical temperature/solar data in long-term deployment, it is not able to react to real-time variations after the deployment. Our adaptive routing algorithm is designed to address post-deployment adjustments. In addition to the normal case that exactly follows the estimated temperature distributions and has no packet loss, we simulate two different scenarios that are representative of potential variations after the deployment:

(1) *Temperature deviation:* To simulate the unexpected temperature and solar irradiance deviation, we download the NSRDB data of year 2010 for sensor placement optimization, and input the traces of year 2020 into *RelIoT* to simulate reliability degradation. For reference, the annual average temperature in the region is increased by 2.4°C between 2010 and 2020.

(2) *Wireless interference:* We assume that there is wireless interference from nearby communicating devices that results in packet losses. We manually place interfering devices near each node in the network. These devices randomly generate interference at irregular intervals. IoT devices operate on unlicensed wireless bands and are therefore susceptible to interference from unrecognized devices using the same band. The interference is usually random and unknown in advance, which cannot be taken into account in optimization.

For each scenario, we use the same placement generated by R-TSH and apply the fixed routing, the original AODV and our *AODV-Rel*. The fixed routing paths are generated by R-TSH assuming that there is no post-deployment variation. The original AODV purely optimizes for the number of hops without considering the reliability.

We simulate a 23-node deployment generated by R-TSH, which is optimal for the assumed ambient temperature distribution and no packet loss. The results for the minimal reliability and operational lifetime of all nodes are presented

TABLE V
COMPARISON OF VARIOUS ROUTING ALGORITHMS ON THE MINIMAL SOH AND ELECTRONICS MTTF (IN PERCENTAGE TO THEIR STANDARD VALUES UNDER TEMPERATURE $T_{ref} = 25°C$) AND THE MINIMAL OPERATIONAL LIFETIME IN MONTHS

| | Method | Min SoH | Min MTTF$_e$ | Min Lifetime |
|---|---|---|---|---|
| Normal | Fixed | **90.4%** | **95.2%** | **63.8** |
| | AODV | 88.9% | 93.0% | 61.2 |
| | AODV-Rel | 89.6% | 94.6% | 63.2 |
| Temp. variation | Fixed | 87.5% | 90.6% | 59.0 |
| | AODV | 86.6% | 88.7% | 56.9 |
| | AODV-Rel | **88.7%** | **92.3%** | **60.5** |
| Wireless interfere. | Fixed | 86.8% | 88.8% | 57.2 |
| | AODV | 86.0% | 88.2% | 56.3 |
| | AODV-Rel | **88.1%** | **91.5%** | **60.0** |

TABLE VI
THROUGHPUT IN KBPS OF THE BOTTLENECK NODE UNDER VARIOUS SCENARIOS

| | Fixed | AODV | AODV-Rel | | |
|---|---|---|---|---|---|
| | | | Normal | Temp. | Interfere. |
| Throughput | 15.00 | 20.00 | 16.16 | 12.24 | 11.77 |

in Table V. We evaluate the *operational lifetime* which refers to the time when reliability degrades below 0.5, that is, the node has 50% probability to fail before that moment. It can be seen that fixed R-TSH routing is the best method under "normal" conditions. This is expected as the R-TSH solution, including both deployment and routing, is optimized for undeviating post-deployment environments. However, adaptive routing improves the R-TSH solution when there is temperature deviation or wireless interference. By using adaptive routing, the bottleneck node (i.e., the node presents minimal reliability) can stay above the specified reliability level for 1.5 and 2.8 months longer at deviated ambient temperature and wireless interference respectively, compared to fixed routing. There is a trade-off for employing either approach: if the environment estimations are perfect and communication is reliable, then fixed routing of R-TSH is optimal. Otherwise, adaptive routing is preferred as it can adapt to changing conditions. The default AODV performs the worst because it always routes through the same nodes for the least number of hops. Therefore, it is not adaptive to temperature or interference variations in the network.

The discrepancy in the results of the compared approaches can be explained by the amount of data routed through the bottleneck node as shown in Table VI. We should note that the bottleneck node is not the same for all approaches. The fixed routing and the default AODV approaches have the same throughput for all scenarios, so we present them with a single entry on the table. AODV routing decisions are purely based on the number of hops, hence there is no change in the amount of data forwarded through the bottleneck node. The throughput, and hence the communication load is lowered by adaptive routing in temperature deviation and wireless interference scenarios. Packet losses cause retransmissions which increase the average power consumption. Adaptive routing avoids sending packets through the bottleneck node because its power margin is low as a result of retransmissions and higher temperature. Therefore, adaptive routing in the temperature variation scenario and in the packet loss scenario have lower throughput

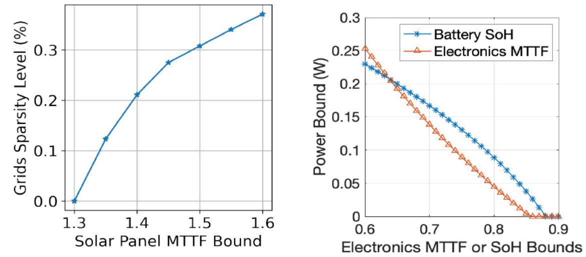


(a) The sparsity level of candidate grids when varying MTTF bounds for solar panels.

(b) The corresponding power bound from battery SoH and electronics MTTF model.

Fig. 9. Impact of reliability bounds on each model.

than the default scenario (AODV-Rel), which are 12.24 kBps and 11.77 kBps, respectively.

### D. Discussion

In this section, we provide more insights by discussing the impact of several key issues.

*1) Impact of Reliability Bounds:* As explained in Section III, our framework includes reliability models for three hardware components: solar panels, electronics and rechargeable batteries. Every deployed node is designed to meet the reliability bounds. Depending on the temperature distribution and reliability bounds, one of the components' reliability plays a dominant role among the three. We experiment with the reliability bounds to evaluate the impact of each model using real-world dataset from NSRDB [13].

We convert the solar panel reliability model to a binary indicator showing the reliability of solar panel installation. If high temperature accelerates failures on a solar panel so that its MTTF drops below a predetermined bound, i.e., $MTTF_{sp} < MTTF_{sp,ref}$, we "disable" the node from candidate grid which increases sparsity. Figure 9(a) depicts the sparsity level of candidate grid when varying $MTTF_{sp,ref}$. Recall that $MTTF_{sp}$ is expressed as a ratio to its standard value under 25 °C. Therefore, Figure 9a indicates that all candidate sites ensure the local $MTTF_{sp}$ is longer than 1.3x of the standard value, under the temperature distribution from NSRDB. In practice, the solar panel model usually provides the weakest reliability bound compared to the rest.

Unlike the solar panel model, both electronics and battery reliability models are calculated from devices' temperature which depends on power consumption and ambient temperature. Suppose that the ambient temperature is 35 °C, which is common in the summer. Figure 9b plots the equivalent power bound to satisfy various SoH and electronics MTTF requirements (i.e., $SoH_{ref}$ and $MTTF_{e,ref}$) as in Eq. (15). The electronics MTTF bound offers the harshest reliability requirement when $SoH_{ref}$ and $MTTF_{e,ref}$ are greater than 0.64, while battery SoH dominates the deployment otherwise.

*2) Temperature Sensitivity Analysis:* We perform temperature sensitivity test to observe the impact of increased temperature on deployment. Using the same setting as in the large-scale simulation, we add up to 6 °C to all sites and observe the number of nodes and reliability violations returned

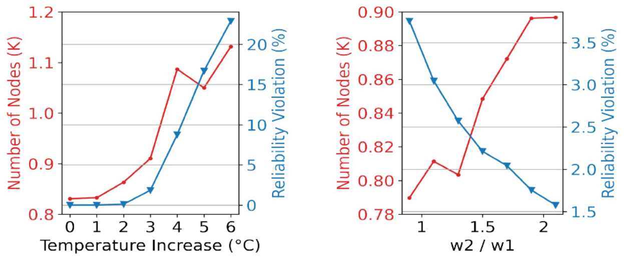


(a) Temperature sensitivity analysis on R-TSH. (b) Weight parameter sensitivity analysis on R-TSH.

Fig. 10. Sensitivity analysis results.

by R-TSH. We set 10K candidate sites and 100 PoIs randomly distributed over the field. We present the average values after 20 trials in Figure 10a. With a temperature increase less than 3 °C, R-TSH keeps reliability constant while more nodes are placed. Once the temperature increase is greater than 3 °C, deploying additional nodes cannot hold back reliability violations. This analysis is based on the weight parameters of R-TSH, which is discussed in the following paragraph.

*3) Weight Parameter Sensitivity Analysis:* The weight parameters $w_1, w_2$ in R-TSH adjust the trade-off between deployment cost and reliability. To study the impact of weight parameters, we use the same setting as the temperature sensitivity test and vary $w_2/w_1$ in R-TSH between 0.9 and 2.1. Figure 10b shows the average deployed nodes and reliability violations after 20 trials. If $w_2/w_1$ is small, the first term in Eq. (17) gains more weight, and thus the deployment cost becomes more critical.

## VII. Conclusion

In this paper, we propose a complete framework for reliability-aware deployment and routing in energy-harvesting IoT networks, including *pre-deployment* sensor placement and *post-deployment* adaptive routing. For sensor placement, we formulate a MILP which minimizes the number of nodes while ensuring reliability, then propose a polynomial heuristic named R-TSH to solve large problems efficiently. For adaptive routing, we design a new reliability-aware routing algorithm based on AODV. Comprehensive simulations using real-world solar irradiance and ambient temperature datasets show R-TSH avoids 15 - 55% of reliability violations with a comparable number of nodes and execution time compared with baselines, while the adaptive routing algorithm further extends the minimal operational lifetime by 1.5 and 2.8 months under temperature deviation and wireless interference.

## References


[1] X. Yu, X. Song, L. Cherkasova, and T. Š. Rosing, "Reliability-driven deployment in energy-harvesting sensor networks," in *Proc. 16th Int. Conf. Netw. Serv. Manag. (CNSM)*, 2020, pp. 1–9.

[2] K. Saravanan, E. G. Julie, and Y. H. Robinson, "Smart cities & IoT: Evolution of applications, architectures & technologies, present scenarios & future dream," in *Internet of Things and Big Data Analytics for Smart Generation*. Cham, Switzerland: Springer, 2019, pp. 135–151.

[3] M. Ayaz, M. Ammad-Uddin, Z. Sharif, A. Mansour, and E.-H. M. Aggoune, "Internet-of-Things (IoT)-based smart agriculture: Toward making the fields talk," *IEEE Access*, vol. 7, pp. 129551–129583, 2019.

[4] "Number of Internet of Things (IoT) connected devices worldwide from 2019 to 2021, with forecasts from 2022 to 2030." Statista. Accessed: Sep. 22, 2022. [Online]. Available: https://www.statista.com/statistics/1183457/iot-connected-devices-worldwide

[5] S. Sudevalayam and P. Kulkarni, "Energy harvesting sensor nodes: Survey and implications," *IEEE Commun. Surveys Tuts.*, vol. 13, no. 3, pp. 443–461, 3rd Quart., 2011.

[6] C. Yang and K.-W. Chin, "On nodes placement in energy harvesting wireless sensor networks for coverage and connectivity," *IEEE Trans. Ind. Informat.*, vol. 13, no. 1, pp. 27–36, Feb. 2017.

[7] X. Zhu, J. Li, M. Zhou, and X. Chen, "Optimal deployment of energy-harvesting directional sensor networks for target coverage," *IEEE Syst. J.*, vol. 13, no. 1, pp. 377–388, Mar. 2019.

[8] "The hidden costs of delivering IIoT services: Industrial monitoring & heavy equipment." Cisco Jasper. Apr. 2016. [Online]. Available: https://www.cisco.com/c/dam/m/en_ca/never-better/manufacture/pdfs/hidden-costs-of-delivering-iiot-services-white-paper.pdf

[9] P. Mercati, F. Paterna, A. Bartolini, L. Benini, and T. Š. Rosing, "WARM: Workload-aware reliability management in Linux/Android," *IEEE Trans. Comput.-Aided Design Integr. Circuits Syst.*, vol. 36, no. 9, pp. 1557–1570, Sep. 2017.

[10] J. R. González, M. Vázquez, N. Núñez, C. Algora, I. Rey-Stolle, and B. Galiana, "Reliability analysis of temperature step-stress tests on III–V high concentrator solar cells," *Microelectron. Rel.*, vol. 49, no. 7, pp. 673–680, 2009.

[11] Y. Zou, X. Hu, H. Ma, and S. E. Li, "Combined state of charge and state of health estimation over lithium-ion battery cell cycle lifespan for electric vehicles," *J. Power Sour.*, vol. 273, pp. 793–803, Jan. 2015.

[12] B. Xu, A. Oudalov, A. Ulbig, G. Andersson, and D. S. Kirschen, "Modeling of lithium-ion battery degradation for cell life assessment," *IEEE Trans. Smart Grid*, vol. 9, no. 2, pp. 1131–1140, Mar. 2018.

[13] "National solar radiation database (NSRDB)." Accessed: Sep. 22, 2022. [Online]. Available: https://maps.nrel.gov/nsrdb-viewer/

[14] K. Ergun *et al.*, "RelIoT: Reliability simulator for IoT networks," in *Proc. Int. Conf. Internet Things*, 2020, pp. 63–81.

[15] K. Ergun *et al.*, "Simulating reliability of IoT networks with RelIoT," in *Proc. 50th Int. Conf. Depend. Syst. Netw. (DSN-S)*, 2020, pp. 25–28.

[16] "ns-3: A discrete-event network simulator for Internet systems." 2022. [Online]. Available: https://www.nsnam.org/

[17] O. Moh'd Alia and A. Al-Ajouri, "Maximizing wireless sensor network coverage with minimum cost using harmony search algorithm," *IEEE Sensors J.*, vol. 17, no. 3, pp. 882–896, Feb. 2017.

[18] M. Rebai, M. Le Berre, H. Snoussi, F. Hnaien, and L. Khoukhi, "Sensor deployment optimization methods to achieve both coverage and connectivity in wireless sensor networks," *Comput. Oper. Res.*, vol. 59, pp. 11–21, Jul. 2015.

[19] M. Elhoseny, A. Tharwat, X. Yuan, and A. E. Hassanien, "Optimizing K-coverage of mobile WSNs," *Expert Syst. Appl.*, vol. 92, pp. 142–153, Feb. 2018.

[20] R. Priyadarshi, B. Gupta, and A. Anurag, "Deployment techniques in wireless sensor networks: A survey, classification, challenges, and future research issues," *J. Supercomput.*, vol. 76, pp. 7333–7373, Jan. 2020.

[21] A. Tripathi, H. P. Gupta, T. Dutta, R. Mishra, K. K. Shukla, and S. Jit, "Coverage and connectivity in WSNs: A survey, research issues and challenges," *IEEE Access*, vol. 6, pp. 26971–26992, 2018.

[22] M. E. Keskin, İ. K. Altınel, N. Aras, and C. Ersoy, "Wireless sensor network lifetime maximization by optimal sensor deployment, activity scheduling, data routing and sink mobility," *Ad Hoc Netw.*, vol. 17, pp. 18–36, Jun. 2014.

[23] X. Yu, K. Ergun, L. Cherkasova, and T. Š. Rosing, "Optimizing sensor deployment and maintenance costs for large-scale environmental monitoring," *IEEE Trans. Comput.-Aided Design Integr. Circuits Syst.*, vol. 39, no. 11, pp. 3918–3930, Nov. 2020.

[24] T. S. Rosing, K. Mihic, and G. De Micheli, "Power and reliability management of SoCs," *IEEE Trans. Very Large Scale Integr. (VLSI) Syst.*, vol. 15, no. 4, pp. 391–403, Apr. 2007.

[25] L. Venkatesan, S. Shanmugavel, and C. Subramaniam, "A survey on modeling and enhancing reliability of wireless sensor network," *Wireless Sens. Netw.*, vol. 5, no. 3, p. 41, 2013.

[26] V. Raghunathan, A. Kansal, J. Hsu, J. Friedman, and M. Srivastava, "Design considerations for solar energy harvesting wireless embedded systems," in *Proc. Int. Symp. Inf. Process. Sens. Netw.*, 2005, pp. 457–462.

[27] D. Newell and M. Duffy, "Review of power conversion and energy management for low-power, low-voltage energy harvesting powered wireless sensors," *IEEE Trans. Power Electron.*, vol. 34, no. 10, pp. 9794–9805, Oct. 2019.

[28] C. Zhuo, D. Sylvester, and D. Blaauw, "Process variation and temperature-aware reliability management," in *Proc. Des. Autom. Test Europe Conf. Exhibit. (DATE)*, 2010, pp. 580–585.

[29] F. Beneventi, A. Bartolini, A. Tilli, and L. Benini, "An effective gray-box identification procedure for multicore thermal modeling," *IEEE Trans. Comput.*, vol. 63, no. 5, pp. 1097–1110, May 2014.

[30] J. Vetter *et al.*, "Ageing mechanisms in lithium-ion batteries," *J. Power Sour.*, vol. 147, nos. 1–2, pp. 269–281, 2005.

[31] A. Maheshwari and N. Chand, "A survey on wireless sensor networks coverage problems," in *Proc. 2nd Int. Conf. Commun. Comput. Netw.*, 2019, pp. 153–164.

[32] I. K. Altinel, N. Aras, E. Guney, and C. Ersoy, "Effective coverage in sensor networks: Binary integer programming formulations and heuristics," in *Proc. IEEE Int. Conf. Commun.*, vol. 9. 2006, pp. 4014–4019.

[33] H.-Y. Zhou, D.-Y. Luo, Y. Gao, and D.-C. Zuo, "Modeling of node energy consumption for wireless S1ensor networks," *Wireless Sens. Netw.*, vol. 3, no. 1, p. 18, 2011.

[34] M. Abo-Zahhad, M. Farrag, A. Ali, and O. Amin, "An energy consumption model for wireless sensor networks," in *Proc. 5th Int. Conf. Energy Aware Comput. Syst. Appl.*, 2015, pp. 1–4.

[35] T. Kozak, W. Maranda, A. Napieralski, G. De Mey, and A. De Vos, "Influence of ambient temperature on the amount of electric energy produced by solar modules," in *Proc. 16th Int. Conf. Mixed Des. Integr. Circuits Syst. (MIXDES)*, 2009, pp. 351–354.

[36] *IBM ILOG CPLEX Optimization Studio, Version*, vol. 12, CPLEX Users Manual, Armonk, NY, USA, 1987, pp. 1987–2018.

[37] V. Chvatal, "A greedy heuristic for the set-covering problem," *Math. Oper. Res.*, vol. 4, no. 3, pp. 233–235, 1979.

[38] C. Perkins, E. Belding-Royer, and S. Das, "RFC3561: Ad hoc on-demand distance vector (AODV) routing," IETF, RFC 3561, 2003.

[39] I. Das, R. N. Shaw, and S. Das, "Analysis of energy consumption of energy models in wireless sensor networks," in *Innovations in Electrical and Electronic Engineering*. Singapore: Springer, 2021, pp. 755–764.

**Xiaofan Yu** (Graduate Student Member, IEEE) received the B.Sc. degree from Peking University, China, in 2018, and the M.Sc. degree from the University of California at San Diego, La Jolla, CA, USA, in 2020, where she is currently pursuing the Ph.D. degree with the Department of Computer Science and Engineering. Her current research interests include designing online lightweight machine learning algorithms and robust sensor deployment strategies for IoT networks.

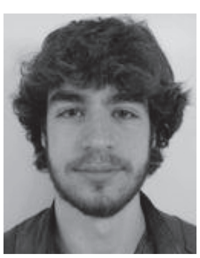

**Kazim Ergun** (Graduate Student Member, IEEE) received the B.Sc. degree in electrical and electronics engineering as a valedictorian from Middle East Technical University, Turkey, in 2017. He is currently pursuing the Ph.D. degree with the Department of Electrical and Computer Engineering, University of California at San Diego, La Jolla, CA, USA. He is a member of the System Energy Efficiency Lab, where he works on optimization and control for the Internet of Things, with the focus on reliability and energy efficiency. His research interests also include edge computing, wireless communications, and machine learning.

**Xueyang Song** received the B.S. degree in computer science from the University of California at San Diego, USA, in 2021. She is currently pursuing the M.S. degree with Department of Computer Science, Stanford University, USA. Her current research interests include machine learning algorithms.

**Ludmila (Lucy) Cherkasova** (Member, IEEE) is a Principal Research Scientist with Arm Research, San Jose, USA. She is focusing on the end-to-end performance, automation, reliability, and cost-effectiveness of the enterprise and IoT systems. Before that for 20+ years she was a Principal Scientist with Hewlett Packard Labs and led to success multiple Research and Development Projects, with prototypes, algorithms, or features implemented in HP products. Her current research interests are in developing quantitative methods for the analysis, design, and management of distributed systems (such as emerging systems for Smart environments, Big Data processing, and next generation data centers). She is the ACM Distinguished Scientist and is recognized by multiple Certificates of Appreciation from Usenix and IEEE Computer Society.

**Tajana Šimunić Rosing** (Fellow, IEEE) received the M.S. degree in engineering management concurrently with the Ph.D. degree from Stanford University, Stanford, CA, USA, in 2001, with the Ph.D. topic "Dynamic Management of Power Consumption."

She is a Professor, a Holder of the Fratamico Endowed Chair, and the Director of System Energy Efficiency Laboratory, University of California at San Diego, La Jolla, CA, USA. From 1998 to 2005, she was a Full-Time Research Scientist with HP Labs, Palo Alto, CA, USA, while also leading research efforts with Stanford University. She was a Senior Design Engineer with Altera Corporation, San Jose, CA, USA. She is leading a number of projects, including efforts funded by DARPA/SRC JUMP CRISP Program with focus on design of accelerators for analysis of big data, DARPA and NSF funded projects on hyperdimensional computing and SRC funded project on IoT system reliability and maintainability. Her current research interests include energy efficient computing, cyber-physical, and distributed systems.